Quantitative 3D Fluorescence Imaging of Single Catalytic Turnovers Reveals Spatiotemporal Gradients in Reactivity of Zeolite H-ZSM-5 Crystals upon Steaming

Zoran Ristanović,[†] Jan P. Hofmann,[†,⊥] Gert De Cremer,[‡,#] Alexey V. Kubarev,[§] Marcus Rohnke,[‖] Florian Meirer,[†] Johan Hofkens,[‡] Maarten B. J. Roeffaers,*,[§] and Bert M. Weckhuysen*,[†]

[†]Inorganic Chemistry and Catalysis, Utrecht University, Universiteitsweg 99, 3584 CG Utrecht, The Netherlands
[‡]Department of Chemistry, KU Leuven, Celestijnenlaan 200 F, B-3001 Leuven, Belgium
[§]Centre for Surface Chemistry and Catalysis, KU Leuven, Kasteelpark Arenberg 23, 3001 Heverlee, Belgium
[‖]Institute of Physical Chemistry, Justus-Liebig-University Giessen, Heinrich-Buff-Ring 58, 35392 Giessen, Germany

S *Supporting Information*

ABSTRACT: Optimizing the number, distribution, and accessibility of Brønsted acid sites in zeolite-based catalysts is of a paramount importance to further improve their catalytic performance. However, it remains challenging to measure real-time changes in reactivity of single zeolite catalyst particles by ensemble-averaging characterization methods. In this work, a detailed 3D single molecule, single turnover sensitive fluorescence microscopy study is presented to quantify the reactivity of Brønsted acid sites in zeolite H-ZSM-5 crystals upon steaming. This approach, in combination with the oligomerization of furfuryl alcohol as a probe reaction, allowed the stochastic behavior of single catalytic turnovers and temporally resolved turnover frequencies of zeolite domains smaller than the diffraction limited resolution to be investigated with great precision. It was found that the single turnover kinetics of the parent zeolite crystal proceeds with significant spatial differences in turnover frequencies on the nanoscale and noncorrelated temporal fluctuations. Mild steaming of zeolite H-ZSM-5 crystals at 500 °C led to an enhanced surface reactivity, with up to 4 times higher local turnover rates than those of the parent H-ZSM-5 crystals, and revealed remarkable heterogeneities in surface reactivity. In strong contrast, severe steaming at 700 °C significantly dealuminated the zeolite H-ZSM-5 material, leading to a 460 times lower turnover rate. The differences in measured turnover activities are explained by changes in the 3D aluminum distribution due to migration of extraframework Al-species and their subsequent effect on pore accessibility, as corroborated by time-of-flight secondary ion mass spectrometry (TOF-SIMS) sputter depth profiling data.
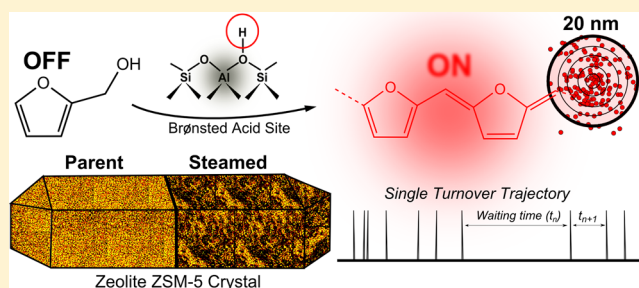
INTRODUCTION

Zeolites represent a very important class of solid acid catalysts utilized in a number of large-scale industrial applications. The unique combination of acidic and shape-selective properties has made zeolites the workhorse in oil refining and petrochemical applications, including fluid catalytic cracking (FCC),[1,2] methanol-to-olefins,[3] isomerization, and alkylation processes.[4] A challenge for the rational design of better-performing zeolites is to tune the number, distribution, and nature of acid sites as well as to facilitate the molecular diffusion of reactants and products via the formation of mesopores. Therefore, improving the catalytic performance of zeolites calls for a deeper understanding of single zeolite particle reactivity.

The Brønsted acidic nature of zeolites is generally associated with bridging hydroxyl protons resulting from isomorphous substitution of Si (IV) by Al (III).[5] The ability to synthesize well-defined zeolite crystals and to tune their Si-to-Al ratio as well as the architecture of microporous voids according to the

application is certainly without parallel in heterogeneous catalysis.[6] However, molecular transport, and therefore the reactivity, in purely microporous zeolite crystals is tremendously hindered by slow diffusion.[7] Steaming of zeolites is the most preferred, simple, and cost-efficient industrial post-treatment method to shorten the effective diffusion pathways and enhance the accessibility of acid sites via the creation of mesopores.[8,9] During this process, dealumination of the zeolite takes place, which inevitably leads to a partial or a complete loss of Brønsted acidity.[10,11] While structural properties and the interconnection of micro- and mesopores can be studied with high-resolution scanning electron microscopy (HR-SEM) and transmission electron microscopy (TEM),[12,13] the acidic properties of zeolites are mainly assessed via bulk measurements, such as solid-state NMR,[14] X-ray absorption spectros-

copy,[15,16] temperature-programmed desorption (TPD), and infra-red (IR) spectroscopy, of numerous probe molecules.[17] Very recent advances in scanning transmission X-ray microscopy (STXM) enabled mapping of Al coordination in 3D with ∼30 nm resolution.[18,19] Microspectroscopic methods that utilize probe molecules such as UV−Vis microscopy,[20] confocal fluorescence microscopy,[21,22] IR microscopy,[23] and coherent Raman spectroscopy,[24−26] provide essential chemical information about reactive acid sites; however, they do so with the limited, micrometer, resolution. As a consequence, inherent intra- and interparticle heterogeneities may pass unnoticed despite significantly altering the catalytic activity in space and time.[26−28] Therefore, in order to understand how the synthesis of zeolite material influences its catalytic performance, it is of fundamental importance to further comprehend the nanoscopic differences in the acidity and reactivity of single zeolite particles.

Single molecule fluorescence microscopy has revolutionized life sciences and the chemical understanding of numerous biological processes. Besides offering the ultimate sensitivity limit of an analytic method, it opens possibilities to overcome the diffraction limited resolution of optical microscopy by localizing single fluorescent molecules with nanometer precision. In the fields of heterogeneous catalysis and material science, several examples have demonstrated the remarkable potential of this technique for visualizing the diffusion of fluorescent molecules in mesoporous materials[29,30] and the reactivity of catalyst particles.[26,31−39] However, despite the fact that there are no obstacles in instrumentation, the application of this method in the field of catalysis is seriously lagging behind its biological applications.[40−42]

In this work, we study the acid-catalyzed oligomerization of furfuryl alcohol (FA) taking place at Brønsted acid sites of individual zeolite H-ZSM-5 crystals. To study the Brønsted acidity of zeolite H-ZSM-5, we used large zeolite crystals as well-defined model systems. These consist of six individual subunits with the orientation of sinusoidal and straight pores differing between the crystal body and edges, often referred to as 90° intergrowths (Figure 1a).[43,44] As a consequence, molecular transport, diffusion, and reactivity change anisotropically throughout the crystal, influencing the overall catalytic performance of an individual catalyst particle.[43]

The concept of nanometer accuracy by stochastic chemical reactions (NASCA) microscopy was previously used to resolve the individual catalytic conversions of FA on individual H-ZSM-5[33] and H-MOR[26] crystals. Using the 3D NASCA approach, we now follow real-time changes in the stochastic dynamics of catalytic turnovers in parent and steamed zeolite H-ZSM-5 crystals. To quantify the effects of steaming post-treatments on the rate of formation of fluorescent products, we monitored the dynamics of catalytic turnovers at three different types of single zeolite crystals that are intentionally chosen to mimic mild and severe steaming processes (typically used to improve molecular diffusion and alter the strength and accessibility of acid sites). According to the procedure of Aramburo et al.,[45] crystals with different degrees of Brønsted acidity and mesoporosity have been prepared, namely, parent crystals (H-ZSM-5-P), with preserved Brønsted acidity and intact microporosity; mildly treated crystals (H-ZSM-5-MT; steamed for 5 h at 500 °C), with induced surface mesoporosity and preserved Brønsted acidity; and severely treated crystals (H-ZSM-5-ST; steamed for 5 h at 700 °C), with a high degree of mesoporosity (surface and bulk) and low Brønsted acidity. Recently, multilaser confocal fluorescence microscopy was used
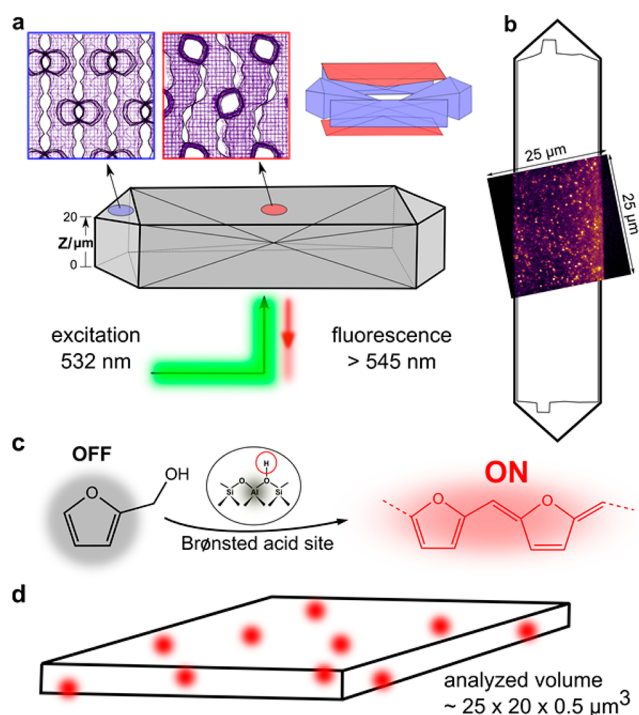
Figure 1. Schematic of the single molecule fluorescence approach used to map in 3D the reactivity of a single H-ZSM-5 crystal. (a) Intergrowth structure of a zeolite H-ZSM-5 crystal indicating the direction of straight and sinusoidal pores in different subunits (color coded). (b) Accumulated image of individual fluorescent products depicted with respect to the size of the zeolite crystal. (c) Formation of fluorescent products (red) upon protonation of FA (black) on a Brønsted acid site. (d) Estimate of the analyzed crystalline volume depicting the 3D distribution of fluorescent molecules (red). Note that the localization precision in the Z-direction is estimated to be ∼500 nm.

to resolve the location of different fluorescent styrene oligomers in the very same types of model H-ZSM-5 crystals.[22]

It will be now shown that the unique sensitivity and spatial resolution of NASCA microscopy enables accurate quantification of the local turnover frequencies in 3D for nanoscopic zeolite domains within individual, parent and steamed, zeolite H-ZSM-5 crystals. This approach can be used to visualize enhanced catalytic activity and large micron-scale heterogeneities in local turnover frequencies of mildly steamed zeolite crystals as well as to measure a significant loss of turnover activity of severely steamed zeolite crystals. Furthermore, the approach allows the stochastic behavior of single catalytic turnovers and their temporal correlations within nanoscopic zeolite domains to be studied. On the basis of this method, it was found that the single turnover kinetics of the seemingly homogeneous parent material proceeds with significant spatial, nanoscale, differences and noncorrelated temporal fluctuations.

■ EXPERIMENTAL SECTION

Synthesis of Zeolite H-ZSM-5-P Crystals in Acidic Form. Large coffin-shaped zeolite H-ZSM-5 crystals (Figure 1a) with an average size of ∼20 × 20 × 100 μm³ and a bulk Si/Al ratio of 17 were used as provided by ExxonMobil (Machelen, Belgium). The synthesis procedure has been reported elsewhere.[45] Organic template molecules (tetrapropylammonium, TPA) were removed by careful calcination (1 °C/min) at 550 °C for 8 h. After template removal, the zeolite crystals were converted into their acidic form by a triple ion-exchange with 10 wt % ammonium nitrate (99+%, Acros Organics) at 80 °C, followed

by 6 h calcination at 500 °C. To avoid residual fluorescence, prior to use, the crystals were activated at 500 °C (1 °C/min) for 24 h in static air.

Steaming Post-treatment of Zeolite H-ZSM-5-MT and H-ZSM-5-ST Crystals. Zeolite H-ZSM-5-P crystals in acidic form have been used for further preparation of steamed samples. Steaming was performed under two sets of conditions, with the intention to simulate mild steaming (H-ZSM-5-MT) and severe steaming (H-ZSM-5-ST) of parent H-ZSM-5-P crystals. Zeolites were heated in a tubular oven to 500 °C (H-ZSM-5-MT) and 700 °C (H-ZSM-5-ST) at a heating rate of 5 °C/min. Further steaming treatment was performed using water-saturated (373 °C) N_2 flow (150 mL/min) for 5 h. Details on the preparation and characterization of the crystals with UV–vis microscopy, confocal fluorescence microscopy, synchrotron-based IR microspectroscopy, atomic force microscopy, HR-SEM, and X-ray photoelectron spectroscopy (XPS) have been reported before.[45]

Wide-Field Fluorescence Setup. Figure 1a presents a schematic of the experimental approach. Single molecule fluorescence experiments were performed using an inverted epifluorescence wide-field microscope (Olympus IX-71), equipped with a 100× oil immersion objective lens (1.4 NA) and a highly sensitive electron multiplying CCD (EMCCD) camera (ImagEM Enhanced C9100-23B, Hamamatsu). Wide-field illumination was achieved by circularly polarized 532 nm light from a diode laser (Excelsior 532, Spectra-Physics). Fluorescent emission was imaged by the EMCCD after passing through a dichroic mirror and a 545 nm long-pass filter to remove the excitation light. The image was expanded by a 3.3× camera lens, resulting in a field of view of $24.6 \times 24.6~\mu m^2$ and $48 \times 48~nm^2$ per pixel. Wide-field images of catalytic turnovers were recorded approximately at the middle of the zeolite crystal (Figure 1b) with a frame rate of 10 images per second.

Experiment. The oligomerization of FA (Figure 1c) was performed on activated zeolite H-ZSM-5 crystals loaded on the top of a cover glass in a reactor designed for liquid-phase experiments. The crystals were exposed to furfuryl alcohol (99%, Sigma-Aldrich), previously diluted in Milli-Q water, to achieve desirable catalytic activity. The optimal concentration of FA for high-resolution imaging was determined in a series of concentration-dependent measurements. The reaction was then monitored by focusing at the surface of the bottom subunit (denoted here as $Z = 0$) or by moving the focus to any provisional focal depth in axial Z-direction up to $Z = 20~\mu m$ (Figure 1a), with the estimated precision of $\pm 0.2~\mu m$. Prior to the experiments, the absence of residual fluorescence was verified on individual crystals. All experiments were performed at room temperature.

Data Analysis. Recorded movies were analyzed with Localizer software[46] developed for Igor Pro (Wavemetrics) and Matlab (MathWorks). Subdiffraction localization of fluorescent events was done by independent segmentation of each frame into emissive spots and background using the approach of Sergé et al.[47] The pixels identified by this segmentation were reduced to a list of initial emitter positions by considering adjacent active pixels as belonging to a single emitter. The locations of these emitters can be determined with subdiffraction limited resolution by fitting a 2D Gaussian using the Levenberg–Marquardt least-squares algorithm as implemented in the GNU Scientific Library. The correct functioning and absence of systematic errors in the algorithm were verified by visual inspection of the processed results.

Emitter Tracking Analysis. The emitter tracking algorithm, as implemented in Localizer software, has been used to correct for the reappearance of fluorescent events in repetitive frames, a necessary step in order to quantify individual turnovers. An iterative procedure was further used to optimize the parameters of the algorithm that take into account the experimental results of single molecule reappearance in subsequent localizations (pixel jump) and blinking of the fluorescent molecule (blinking time). Optimal values of 55 nm pixel jump and 0.5 s blinking time were found to be a good experimental correction for the summed effects of photobleaching, blinking, localization precision, and molecular diffusion (Supporting Information S1). The large majority of fluorescent events can be localized with an estimated lateral precision of 17 ± 9 nm (Supporting Information

S2). However, the optimized algorithm accounts also for the extremes in the localization efficiency (e.g., when one molecule appears in many consecutive frames) in order to eliminate artificially generated hotspots of reactivity. This approach is sensible considering that the probability of consecutively finding two fluorescent molecules within the diameter of 55 nm is very low.

TOF-SIMS Analysis of Al Distribution. The time-of-flight secondary ion mass spectrometry (TOF-SIMS) experiments were carried out on a TOF-SIMS 5.100 machine (ION-TOF GmbH, Münster, Germany). For data evaluation, SurfaceLab 6.3 was used. The UHV chamber had a base pressure $< 5 \times 10^{-10}$ mbar, which increased during the work on the zeolite H-ZSM-5 crystals to 10^{-8} mbar. Charge compensation of the nonconducting samples was provided by an electron flood gun. Samples were transferred into the UHV chamber of the TOF-SIMS machine without further preparation. The crystals were sprinkled on conductive 0.2 mm thick polycarbonate stickers with graphite powder mixed in the adhesive, as is commonly used for scanning electron microscopy (Plano GmbH, Wetzlar, Germany). All measurements were conducted at room temperature.

TOF-SIMS surface analysis was done using Bi^+ primary ions ($E(Bi^+) = 25$ keV, $I(Bi^+) = 0.40$ pA). For sputter depth profiling, O_2^+ ions ($E(O_2^+) = 1$ keV, $I(O_2^+) = 325$ nA) were used. The sputter area was $120 \times 120~\mu m^2$. The analysis itself was carried out in an area of $120 \times 120~\mu m^2$ (128×128 pixels) with Bi^+ ions in low-current bunch mode (lateral resolution $\sim 2~\mu m$) in the center of the sputter area. The data were obtained by periodic cycling of 2 s of Bi^+ analysis, 5 s of O_2^+ sputtering for the parent crystal and 10 s for the steamed crystals, and 1 s resting time. The TOF analyzer was operated in positive ion mode. For evaluation of the Si^+/Al^+ secondary ion ratio, the mass spectra were reconstructed based on the signal originated from the defined region of interest. It is important to note that the obtained ratio is not an atomic Si/Al ratio but merely the Si^+/Al^+ secondary ion ratio. Niemantsverdriet reported the secondary ion yields of Si^+ and Al^+ from their pure oxides as being 0.58 and 0.7, respectively.[48] On the basis of the ratio of the secondary ion yields ($Y_{ox}(Si^+)/Y_{ox}(Al^+) = 0.83$), a calibration of the Si/Al ratio could be achieved. We noted small variations in the absolute values of Si^+/Al^+ signals recorded for different crystals. However, the trends of the obtained curves Si/Al ratio vs sputter time or sputter depth remained unchanged. The sputter depth was estimated by measuring the sputtered crystals by confocal microscopy height profiling. An average sputter depth of $10 \pm 2~\mu m$ was achieved, indicating that the middle of the crystal has been reached. A coarse calibration of the depth profiling data was assumed based on linear relation between sputter time and sputter depth.

■ RESULTS AND DISCUSSION

Single Molecule Fluorescence Microscopy. The acidic properties of H-ZSM-5 crystals were tested using the oligomerization of furfuryl alcohol (FA), a fluorogenic reaction used to probe the Brønsted acid sites of zeolites H-ZSM-5 and H-MOR.[26,33,39] FA oligomerization at the Brønsted acid sites of zeolite H-ZSM-5 leads to the formation of highly fluorescent oligomeric carbocations (Figure 1c). For the oligomerization mechanisms, the reader is referred to Supporting Information Scheme S1. Fluorescent products are efficiently excited by 532 nm laser light, followed by subsequent detection of the fluorescence emission of the product molecules (Figure 1b). The steric confinement of the product molecules in the zeolite pores contributes to their excellent fluorescence properties and enhanced contrast with respect to that of the molecules that have diffused into the bulk solution. Supporting Information Movie S1 illustrates that fluorescent events are taking place at different focal depths with respect to the surface of the zeolite crystal, a consequence of intracrystalline diffusion and the stochastic nature of the catalytic process. Their location in the axial direction can be determined with an estimated precision on the order of ~500 nm, a value that is used in the later

quantification analysis.[36] On the basis of this, it can be approximated that the single molecule events are simultaneously recorded within a crystalline volume of approximately $25 \times 20 \times 0.5 \ \mu m^3$, where $25 \times 20 \ \mu m^2$ represents a projected area of the crystal (Figure 1d). Within this volume, we estimate 2.7×10^{11} Brønsted acid sites if all Al atoms are considered to be catalytically active. Clearly, the concentration of FA is a critical variable to achieve turnover activity optimal for imaging. Low reaction rates, typically in the range of 1−1000 detected product molecules per second and per crystal section, enable successful quantification of individual fluorescent events and prevent simultaneous spatial overlapping of the fluorescent product molecules (Figure 2a).
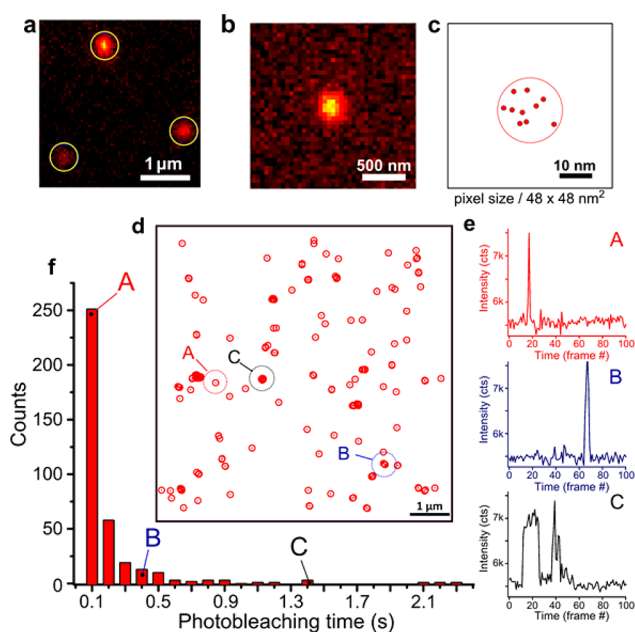

Figure 2. NASCA localization approach. (a) Three isolated catalytic events (bursts), as identified by the 2D Gaussian localization algorithm. (b) A single burst, as detected by the EMCCD camera, and (c) subsequent localization of a fluorescent event appearing in 10 consecutive frames. The red circle denotes a diameter of 20 nm, indicating the lateral spatial precision of the method. (d) High-resolution map of fluorescence activity based on 100 consecutive frames. (e) Typical fluorescence trajectories of the events shown in (d). (f) Histogram of the photobleaching times for 370 single molecules.

Each fluorescent reaction product manifests on the detector through a fluorescent burst with an intrinsic point spread function (PSF) of ∼230 nm at FWHM (Figure 2b). However, the lateral localization precision of the method is substantially improved by fitting the PSF of a fluorescent molecule by a 2D Gaussian localization algorithm, resulting in a typical localization precision of 17 ± 9 nm (Figure 2c and Supporting Information S2). By following this localization approach for many repetitive frames, single turnovers can be localized in 3D for any specific focal depth within the crystal Z-axis (20 μm, as illustrated in Figure 1a, with the axial (Z) localization precision estimated to be ∼500 nm). This results in reactivity maps that indicate the precise 2D location of detected fluorescent events (Figure 2d). Fluorescent events may reappear in several consecutive frames before they permanently photobleach (Figure 2e). The histogram of photobleaching lifetimes shows

that the majority of fluorescent products are photobleached within a short time interval of 0.5 s (Figure 2f). Fast photobleaching of fluorescent products is essential for the quantification of the catalytic turnovers. Furthermore, the photobleaching prevents fast accumulation of the background fluorescence and enables stable monitoring over an extended period of time. The analysis of the products' brightness did not indicate a substantial attenuation of fluorescence in the deeper regions of the single zeolite crystals. Hence, the single molecules products were efficiently localized despite a slight increase in the scattered background signal, mostly originating from the side subunits (Supporting Information S3).

In our analysis, each fluorescent burst, that repeats in consecutive image frames and within a localization diameter of 55 nm, counts as one catalytic turnover. However, once the product is photobleached we account for the formation of new fluorescent molecules that may appear in this area. To account for the effects of the burst reappearance in multiple frames and formation of new product molecules we have used the emitter tracking algorithm, as described in the Experimental Section and the Supporting Information S1.

Time-Dependent Quantification of the Stochastic Single Turnover Dynamics. To follow the dynamics of catalytic turnovers taking place in the micropores of zeolite H-ZSM-5-P crystals, we optimized the reaction conditions that favor efficient detection of the reaction products, i.e., the photobleaching of the catalytically formed fluorescent products is compensated by the formation of novel reaction products catalyzed by abundantly present Brønsted acid sites. Using the developed method, it is possible to temporally resolve and quantify single catalytic turnovers that simultaneously take place within the analyzed volume. This is illustrated in Figure 3a, where the turnover rate is monitored over 4 h of catalytic
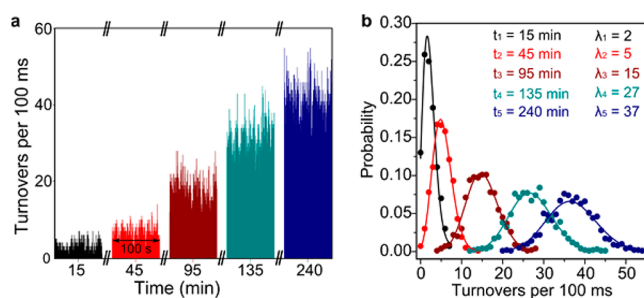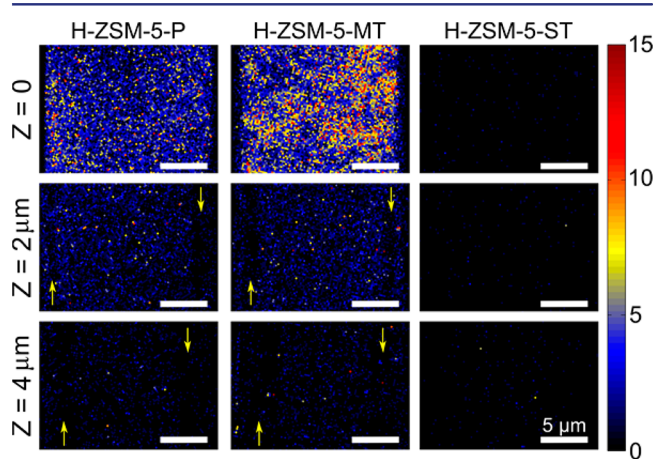

Figure 3. Single turnover stochastics of the oligomerization reaction monitored at the surface of the H-ZSM-5-P single crystal for 4 h in a 5.75 mM solution of FA. (a) Total number of detected turnovers per frame as a function of time. Each time interval is 100 s. Note the large time gaps between the measurements. (b) Poisson distributions of the corresponding color-coded trajectories presented in (a), including the Poisson parameter λ.

reaction taking place close to the surface of the single H-ZSM-5-P crystal. The number of catalytic turnovers counted over 100 ms time intervals follows a Poisson distribution with an increased broadening and shift toward higher mean values as a function of time (Figure 3b).

The parameters of the Poisson distribution describe the stochastic nature of the catalytic process for an arbitrary region of interest, which is ultimately limited by the resolution of our method. Figure 3 suggests that the turnover rates fluctuate stochastically around mean values that are a function of time and the concentration of the reaction intermediates. The latter

is limited by the slow intracrystalline diffusion of FA molecules into microporous voids of H-ZSM-5. Therefore, in order to study the reactivity in deeper crystalline regions, reaction conditions should be optimized to yield moderate turnover rates. We found that a 5.75 mM solution of FA is an optimal concentration to quantify single turnover dynamics in 3D for the studied zeolite crystals.

3D Imaging of Steaming Effects on Reactivity. Using the NASCA approach, we compared the 3D reactivity of the parent zeolite H-ZSM-5-P crystals with those of the mildly steamed H-ZSM-5-MT and severely steamed H-ZSM-5-ST zeolite crystals. Figure 4 summarizes the accumulated high-
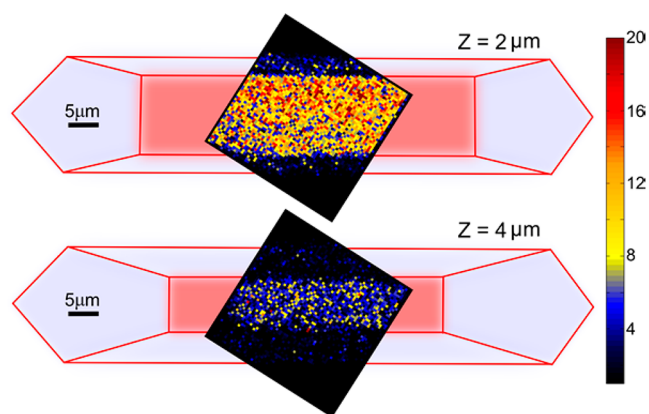

Figure 5. Models of the H-ZSM-5 intergrowth structure: red (top/bottom subunits), straight pores run parallel to the image plain; blue (side subunits), straight pores run perpendicular to the image plain. The overlaid single molecule maps indicate differences in reactivity for planes that are 2 and 4 μm below the surface, after 2.5 h in a 5.75 mM solution of FA. Color bar: turnovers per 800 × 800 nm^2.

Figure 4. Single molecule reactivity maps for H-ZSM-5-P, H-ZSM-5-MT, and H-ZSM-5-ST crystals recorded at three different focal depths (Z = 0 (surface), 2, and 4 μm). Reactivity is accumulated for 1000 frames after 3 h of reaction in a 5.75 mM solution of FA. Yellow arrows indicate the regions with lower reactivity due to a different crystallographic orientation of the subunits. Color bar: turnovers per 200 × 200 nm^2.

resolution reactivity maps, taken after 3 h of reaction at the middle of the three zeolite crystals, for three different focal depths, Z = 0 (surface), 2, and 4 μm, below the surface. The reactivity maps qualitatively suggest the following order of reactivity: H-ZSM-5-MT > H-ZSM-5-P ≫ H-ZSM-5-ST.

Three important conclusions follow from Figure 4. First, mild steaming increases the single turnover activity in the near-surface regions of a single zeolite crystal and induces clearly visible spatial inhomogeneities in reactivity. Second, severe steaming greatly reduces the turnover activity at all focal depths. Finally, reactivity maps at Z = 2 and 4 μm reveal regions of lower fluorescence activity that are a consequence of a different pore orientation in the crystal subunits, as indicated by yellow arrows in Figure 4. From this point on, we will further elaborate on these observations in a quantitative manner by measuring spatiotemporal changes in the turnover frequencies of zeolite domains.

Influence of Structural Anisotropy on the Catalytic Performance of H-ZSM-5 Crystals. The impact of the intergrowth structure on reactivity can be clearly visualized when a sufficient quantity of single molecule products is accumulated in inner regions of the H-ZSM-5 crystal, as illustrated for Z = 2 and 4 μm (Figure 5).

It is striking that the formation of linear fluorescent oligomers proceeds mainly along the straight pores of the zeolite H-ZSM-5-P crystal even though the access to the crystalline bulk of the top/bottom subunits is mainly provided

via sinusoidal pores (Figure 1a).[33] This implies that the circularly polarized laser light interacts predominantly with the transition dipole moments of fluorescent products oriented along the straight pores of zeolite H-ZSM-5. Likewise, the molecules that are aligned within the straight pores of the side subunits (Figure 5) are not efficiently excited with the perpendicular vector component of the laser light and hence these subunits are not taken into account in our quantitative analysis. A strong dependence of the recorded signal from the crystalline anisotropy and the preferential orientation of the guest molecules has been observed on several occasions for H-ZSM-5 and H-MOR crystals using different microscopic techniques.[22,25,26,49]

3D Quantification of the Single Catalytic Turnovers. We have further examined the 3D reactivity profiles of FA in order to provide a complete quantitative picture of the effect of steaming on Brønsted reactivity. Figure 6 illustrates the temporal evolution of the normalized turnover activities, recorded for the parent (H-ZSM-5-P), mildly steamed (H-ZSM-5-MT), and severely steamed (H-ZSM-5-ST) zeolite crystals at four different focal depths. The most notable difference in reactivity of the parent H-ZSM-5-P and mildly steamed H-ZSM-5-MT zeolite crystals is in the surface regions (depth Z = 0). The reactivity profiles evidence slow intracrystalline diffusion of FA, with most of the fluorescent events detected within the 500 nm near-surface layers of the single crystals. The initial uptake of FA molecules and the subsequent oligomerization in H-ZSM-5-MT proceeds faster and reaches a 4 times higher reaction rate after 1 h of reaction than that for H-ZSM-5-P. The reactivity profile of H-ZSM-5-P shows a longer induction period and reaches a maximal turnover activity of 0.63 turnovers per μm^3 per second. This value is about 1.8 times lower than that for H-ZSM-5-MT after 4 h (Figure 6). The surface turnover rates of the measured regions indicate an improved accessibility of the H-ZSM-5-MT crystals achieved by mild steaming. It is worth noting that the H-ZSM-5-MT crystals show consistently higher near-surface turnover rates than those of H-ZSM-5-P crystals. However, the reaction rates recorded at Z = 2 μm do not differ significantly, indicating that mild steaming does not substantially affect the inner crystalline regions of the zeolite material. In contrast to surface turnover rates for both parent and mildly steamed
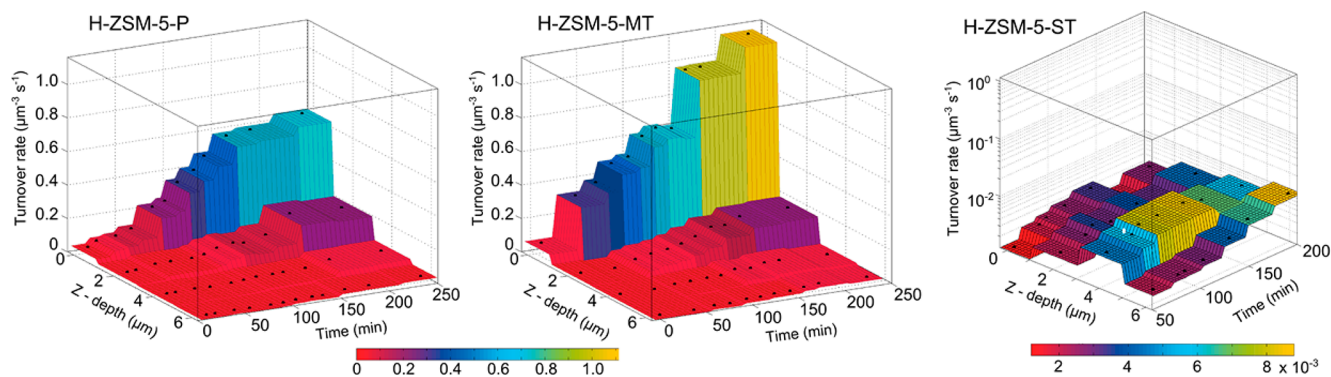
Figure 6. Normalized turnover activities of zeolites H-ZSM-5-P, H-ZSM-5-MT, and H-ZSM-5-ST in a 5.75 mM solution of FA plotted as a function of time and focal depth Z. The turnover rates are calculated and normalized for the top subunit (see Figure 5) in order to eliminate the polarization effect and higher background scattering from the side subunits. The first two experimental points for the H-ZSM-5-MT crystal (after 5 and 42 min) were recorded from two different crystals. The color bars indicate turnover rates, as plotted in the 3D graphs. Note the logarithmic axis for H-ZSM-5-ST. The black dots in the 3D graphs indicate the experimental values.

zeolite crystals, severely steamed H-ZSM-5-ST crystals showed 460 times lower surface turnover rate than that of H-ZSM-5-MT, without notable time-dependent changes. Furthermore, the turnover rates at $Z = 4$ μm are 3 times higher than those at $Z = 0$ (turnover rate of 2×10^{-3} turnover per μm^3 per second), suggesting a drastic change in the amount and distribution of active Brønsted acid sites upon severe steaming.

Measured turnover rates are the summed result of mass transfer limitations and the concentration of accessible acid sites. However, the acid sites of H-ZSM-5-P are not homogeneously distributed throughout the crystal and change further upon steaming post-treatments. A recent micro-X-ray diffraction (μ-XRD) and time-of-flight secondary ion mass spectrometry (TOF-SIMS) study of large zeolite H-ZSM-5 crystals indicated that there is a strong gradient in aluminum concentration (often referred to as Al zoning) present in parent H-ZSM-5-P crystals.[44]

To corroborate the catalytic activity of the studied zeolite crystals with the changes in Al concentration, all three samples were subjected to TOF-SIMS sputter depth profiling measurements (Figure 7). As expected from the surface turnover activity profiles and previous HR-SEM and XPS sputter depth profiling measurements,[45] the most remarkable difference in aluminum distribution can be noticed in the near-surface regions of the crystals. Parent H-ZSM-5-P crystals typically show a depletion of aluminum in a surface layer of approximately 50 nm (first sputter depth profiling point), whereas mildly and severely treated H-ZSM-5-MT and H-ZSM-5-ST crystals exhibit significant Al enrichment in this region (Figure 7). These differences in the surface distribution of aluminum help to understand the observed trends in the reactivity measured by the single molecule fluorescence method. The lower reaction rates in the surface region of the parent crystals are related not only to slow molecular diffusion in H-ZSM-5-P but also to the presence of a silicalite layer at the surface (a Si/Al ratio of 160 has been measured by XPS)[45] that may significantly hinder reactivity.[43] This explains the initially low turnover rates recorded at the surface of H-ZSM-5-P crystals. In contrast, a mild steaming treatment creates extraframework aluminum species in the surface region but does not affect inner regions of the zeolite material, as observed by HR-SEM.[45] This is also an indirect indication of the formation of mesoporous defects in the surface layers of H-ZSM-5-MT crystals that are responsible for enhanced diffusion
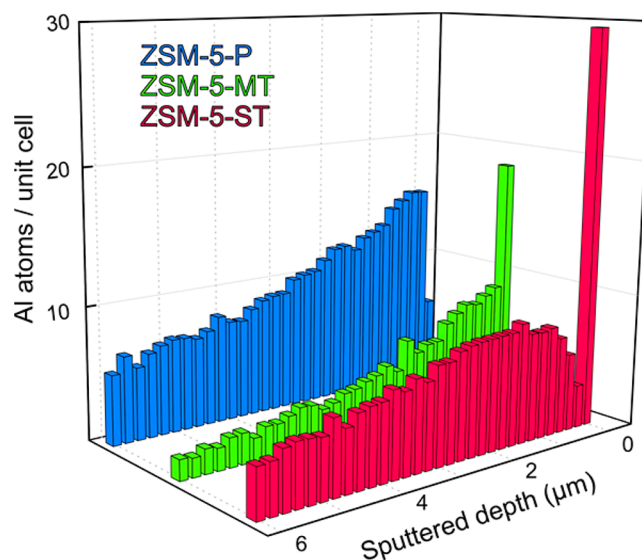
Figure 7. Aluminum TOF-SIMS sputter depth profiles for single zeolite crystals: H-ZSM-5-P (blue), H-ZSM-5-MT (green), and H-ZSM-5-ST (red). The approximate number of Al atoms is calculated on the basis of the TOF-SIMS response of the Si^+/Al^+ signal with respect to 96 T atoms per unit cell of zeolite H-ZSM-5.

and higher single turnover rates, despite a loss in the number of Brønsted acid sites due to dealumination. It should be noted here that, apart from the differences in the near-surface layers, we observe very similar trends in the TOF-SIMS depth profiles of both H-ZSM-5-P and H-ZSM-5-MT. However, the absolute values for measured Si/Al ratio vary from crystal to crystal, as visible in Figure 7, where the concentration of Al atoms seems to be lower for H-ZSM-5-MT.

Measured TOF-SIMS profiles indicate only the total concentration of Al atoms, and not all of them are necessarily tetrahedrally coordinated and incorporated in the framework of zeolite; hence, not all of them are necessarily catalytically active. The example of severely steamed crystals strongly illustrates this point. Recorded turnover frequencies of H-ZSM-5-ST are significantly lower than those for H-ZSM-5-P and H-ZSM-5-MT. This can be rationalized by an abundance of extraframework Al species formed upon severe steaming. The TOF-SIMS Al depth profile indicates that aluminum is still present within the crystal but does not provide Brønsted acidity necessary for

the oligomerization reaction. The first experimental point in the TOF-SIMS profile of H-ZSM-5-ST indicates the deposition of aluminum in the surface layer of the zeolite crystal, most probably due to the high degree of dealumination that is visible up to ~1 μm of the depth profile. In marked contrast, the reactivity observed in the surface layer of H-ZSM-5-ST is very low and cannot be correlated with the concentration of aluminum determined by TOF-SIMS. Remarkably, the observed Al zoning of the H-ZSM-5-P single crystals has a profound effect on the degree of dealumination upon mild and severe steaming, as H-ZSM-5 zeolite with lower Al content is more resistant to dealumination.[50] Therefore, mild steaming will lead to selective dealumination mostly in the surface regions of the H-ZSM-5-MT crystals, where Al has the highest initial concentration. Similarly, severe steaming affects more surface regions of H-ZSM-5-ST crystals than it does deeper parts, where we consistently observe several times higher turnover rates.

High-Resolution Imaging of the Surface Activity. The NASCA method can further provide in-depth insights into the spatiotemporal changes taking place in nanoscopic domains of H-ZSM-5-P and H-ZSM-5-MT. The question arises as to whether the surface of a zeolite crystal is homogeneously affected by the mild steaming method. A closer look into the surface high-resolution reactivity maps of the H-ZSM-5-P and H-ZSM-5-MT zeolite crystals, presented in Figure 4, indicates substantial differences in the spatial distribution of catalytic turnovers. These differences become highly visible when the crystals are exposed to a higher concentration of FA (10−30 mM), enabling fast accumulation of catalytic turnovers. Qualitatively, the reactivity of H-ZSM-5-P was macroscopically homogeneous on a micrometer length scale (Figure 8a), whereas the surface of H-ZSM-5-MT shows significant heterogeneities in reactivity (Figure 8b). To quantify the extent of those differences, the high-resolution maps from Figure 8a,b were divided into 384 × 384 nm² (8 × 8 binned pixels) regions, as illustrated in Figure 8. Such regions are used to construct the histograms of the turnover activity, as presented for H-ZSM-5 P (Figure 8c) and H-ZSM-5-MT (Figure 8d). While H-ZSM-5-P has a fairly narrow distribution of turnover rates determined for 384 × 384 nm² regions of interest, H-ZSM-5-MT shows a broad reactivity histogram with regions of high and low reactivity spanning nearly 1 order of magnitude. A TOF-SIMS sputter depth profile of the mildly steamed crystal (Figure 7) indicates the deposition of extraframework Al species in the near-surface regions of H-ZSM-5-MT crystals. Therefore, a nonuniform turnover activity of the nanoscopic domains of H-ZSM-5-MT could be related to large differences in the accessibility of Brønsted acid sites caused by the migration of Al and blockage of micropores. Such near-surface layers of extreme heterogeneity seem to be responsible for the large transport barriers that may significantly affect the uptake of molecules and unevenly reduce the local permeabilities.[51,52]

The high-resolution map of turnover activity of H-ZSM-5-P (Figure 8a) indicates observable nanoscopic differences in reactivity even for the parent zeolite crystal. The scatter plot in Figure 9a shows the locations of individual catalytic turnovers for a 2.4 × 2.4 μm² region of interest indicated in Figure 8a. The inhomogeneous distribution of catalytic turnovers in Figure 9a could be a consequence of the stochastic nature of the process, which is described by Poisson statistics in Figure 3. To verify this hypothesis, we have simulated a scatter plot that
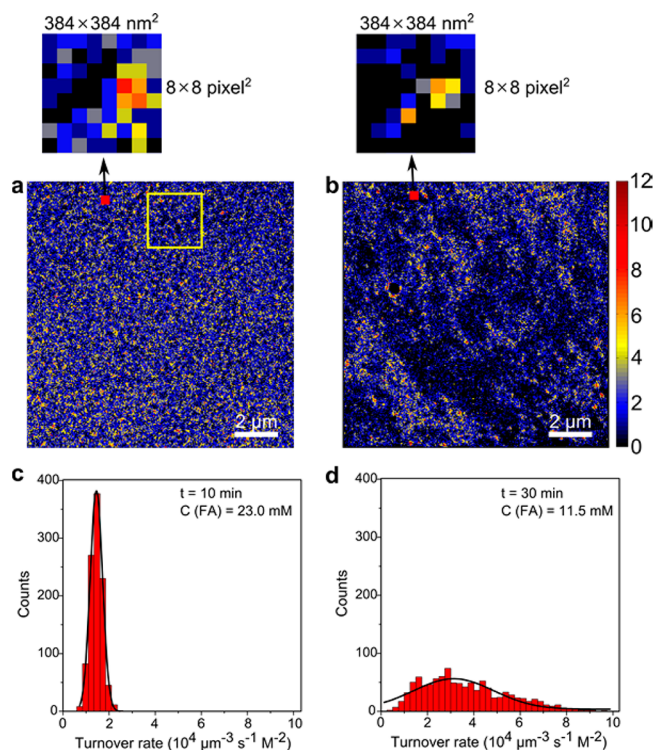

Figure 8. High-resolution imaging of accessible acid sites. (a, b) High-resolution images of surface reactivity based on movies (2000 frames) for (a) a H-ZSM-5-P crystal in a 23 mM solution of FA and (b) a H-ZSM-5 MT crystal in a 11.5 mM solution of FA. The color bar denotes the number of detected turnovers per 48 × 48 nm². Insets marked with arrows indicate high-resolution images of 384 × 384 nm² domains, used for calculating the histograms displayed in (c) and (d). The yellow square in (a) indicates a region of interest used to construct the scatter plot in Figure 9a. (c, d) Corresponding histograms of turnover activity, calculated from 384 × 384 nm² binned regions in (a) and (b) and normalized to the molar concentration of FA, for (c) H-ZSM-5-P and (d) H-ZSM-5-MT.

describes a completely random, stochastic process (Figure 9b). Because the scatter plots are constructed based on the identical number of catalytic turnovers (3709), we would expect a similar distribution of nearest-neighbors (NN) for both H-ZSM-5-P and the simulated pattern.

The histogram in Figure 9c does not support the hypothesis of randomness. The number of NNs in a radius of 100 nm calculated for H-ZSM-5-P suggests a substantial deviation from the simulated random distribution of catalytic turnovers. The histograms for a smaller NN radius (20−50 nm) did not indicate a clear difference in the number of NN catalytic turnovers. Furthermore, increasing the radius of NN analysis to 500−700 nm leads to very similar NN histograms (Supporting Information S4). The observed heterogeneities in reactivity could be a direct consequence of intrinsic differences in the surface accessibility and acidity introduced to the zeolite framework during the synthesis, ion exchange, or activation. In comparison to the NN distribution for H-ZSM-5-P, a histogram of NN distribution for H-ZSM-5-MT shows significant deviation from the simulated pattern (Figure 9d and Supporting Information S5).

The observed changes in reactivity for the H-ZSM-5-P crystals can be resolved with a temporal resolution of 100 ms per frame. We studied the reactivity of the zeolite domain presented in Figure 8a and divided it into 784 smaller domains
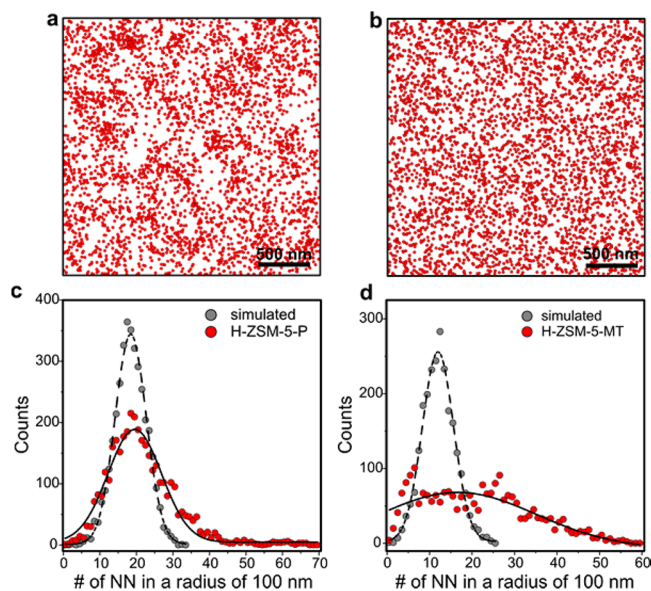
Figure 9. (a, b) Scatter plots of reactivity reconstructed for (a) the H-ZSM-5-P crystal and the region of interest indicated in Figure 8a (yellow square) and (b) a simulated, random scatter plot. Each dot in the scatter plots represents one catalytic turnover. (c, d) Histograms of the number of nearest-neighbors (NN) detected within a radius of 100 nm. (c) Comparison of H-ZSM-5-P and the simulated pattern, calculated from (a) and (b). (d) Comparison of H-ZSM-5-MT and the corresponding simulated pattern (see Supporting Information S5 for the corresponding scatter plots).

with a lateral size of 384 × 384 nm² (Figure 8a). This size was chosen on the basis of the observed density of catalytic events. Smaller domains can be analyzed in a similar manner, but they yield low numbers of detected events per domain. By applying the described quantification procedure, we reconstructed turnover trajectories of all analyzed domains. A digital single turnover trajectory of an exemplified region of interest is shown in Figure 10a.

Each turnover trajectory can be described by the time between subsequent catalytic events, denoted here as waiting time. This parameter was used in single enzyme kinetics to derive memory effects in enzyme conformation dynamics.[53−55] A typical turnover trajectory of a zeolite domain illustrates the stochastic appearance of waiting times (Figure 10b). We compared the turnover trajectories and the resulting cumulative sums of turnovers of all 784 analyzed domains. A selection of five trajectories that differ significantly in their reactivity is shown in Figure 10c. It is evident that individual zeolite domains within a single zeolite particle may differ significantly in their average turnover frequencies.

The distribution of individual waiting times follows the exponential decay function for all analyzed turnover trajectories (Figure 10d), whereas the parameters of the distribution change with turnover frequencies recorded at individual zeolite domains. The question arises as to whether these fluctuations in waiting times have a temporal correlation component, i.e., whether the appearance of two consecutive waiting times can be statistically correlated to temporal changes in the oligomerization reaction mechanism. A summed 2D histogram of adjacent waiting times (t_n and t_{n+1}) calculated for all analyzed trajectories shows a symmetrical distribution of pairs of waiting times (Figure 10e). This distribution describes stochastic behavior of the single turnover trajectories, where higher
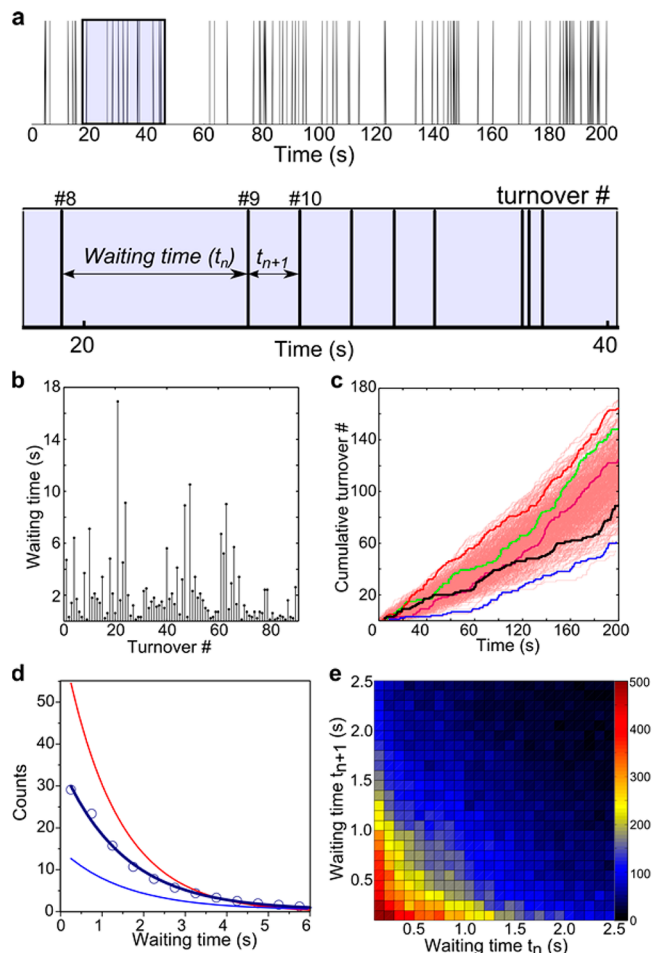
Figure 10. (a) Single turnover trajectory recorded for a 384 × 384 nm² zeolite domain. Inset: definition of the waiting time as the time between two subsequent catalytic turnovers. (b) Waiting time trajectory reconstructed from (a). (c) Evolution of turnover numbers for five exemplified zeolite domains: the black line is derived from (b), and the red lines in the background represent all 784 trajectories. (d) Mean distribution of waiting times calculated for all 784 surface domains (dark blue). The blue and red lines denote the fitted exponential decays of the waiting time histograms for the blue and red trajectories in (c), respectively. (e) 2D conditional histogram of consecutive waiting times recorded at t_n and t_{n+1}. The color bar indicates the occurrence of pairs of waiting times.

turnover rates may be followed with the longer time intervals of low activity. As a test of time-correlated features, we have examined the 2D difference histograms (Supporting Information Figure S6) and the autocorrelation functions of recorded waiting time trajectories (Supporting Information Figure S7). Similar kinetic studies performed earlier for enzymes[53,54,56] and nanoparticles[32] found a correlation of catalytic turnover frequencies in time due to conformational and surface reconstruction changes. Our analysis did not show the presence of similar correlation effects in H-ZSM-5, most probably due to the significantly different nature of the catalytic processes taking place at enzymes and nanoparticles. Very low turnover rates over large zeolite domains, as compared to the size of enzymes and nanoparticles, may not be sufficient to study dynamic disorder at the present time/space scales. However, the reasons for the observed behavior could be well-explained by the interplay of diffusion and the Langmuir−Hinshelwood adsorption−reaction mechanism, taking into account the

complexity of the overall process that may lead to the nonperiodic, chaotic oscillations in reactivity.[57−59]

We note here a remarkable observation related to measuring the turnover frequency of a single catalyst particle. By definition, the turnover frequency is calculated with respect to the total number of catalytically active sites.[6] While the rate of formation of product molecules can be precisely calculated with the NASCA method, the local number of catalytically active sites (and not the local Al concentration) cannot be directly measured in 3D on the same length scales. However, stimulated Raman microscopy with probe molecules recently demonstrated this information at diffraction limited resolutions.[26] The reactivity of zeolite H-ZSM-5 is measured under conditions of extremely low turnover frequencies. Taking into account the maximum in recorded reactivity of 10 events per μm^3 per second (which corresponds to a reaction rate of 1.7×10^{-8} mol dm^{-3} s^{-1} for detected fluorescent products) and a bulk Si/Al ratio of 17, the average recorded turnover frequency of the reaction is in the order of 10^{-8} s^{-1}. In comparison, typical turnover frequencies recorded at a bulk level in zeolites are on the order of 10^{-3} s^{-1}, marking a difference of at least 5 orders of magnitude. The practical upper limit of the NASCA technique applied to studied zeolite crystals is close to measured values, since a higher reactivity of the probe molecules would lead to the fast accumulation of bursts that could not be optically resolved anymore. In practice, the window of turnover values that can be recorded for the studied zeolite H-ZSM-5 crystals ranges from 10^{-12} to 10^{-8} s^{-1}, representing more than 4 orders of magnitude difference in reactivity. In principle, even lower turnover numbers can be determined at the expense of longer acquisition times.

CONCLUSIONS

We have quantified in 3D the effect of steaming post-treatments on the catalytic performance of individual H-ZSM-5 crystals using the high sensitivity and spatiotemporal resolution of single molecule super-resolution fluorescence microscopy. Mild steaming of H-ZSM-5 crystals at 500 °C altered surface porosity via dealumination and notably enhanced accessibility and reactivity; however, this also causes a highly heterogeneous distribution of accessible acid sites at the macroscopic level. Further steaming at 700 °C led to a significant loss of Brønsted acidity and a 2 orders of magnitude lower average turnover frequency. The results were further explained by measuring TOF-SIMS sputter depth profiles of Al distribution. Surface diffusion barriers of the parent zeolite crystals were attributed to the depletion of Al in the surface region of the material, whereas changes in the 3D distribution of Al upon steaming significantly affected the surface accessibility and reactivity of mildly steamed crystals. Finally, the correlation analysis of waiting times between subsequent turnovers pointed toward significant temporal fluctuations and differences in the turnover frequencies of nanoscopic zeolite domains of the parent material. The obtained results demonstrate the importance of single turnover, single catalyst particle studies in unraveling the complex diffusion−reactivity interplay taking place in hierarchical zeolite-based catalyst materials.

ASSOCIATED CONTENT

Ⓢ Supporting Information

Single molecule fluorescence movie, mechanism of the probe reaction, optimization of the localization parameters, NN analysis, and autocorrelation analysis of the turnover trajectories. This material is available free of charge via the Internet at http://pubs.acs.org.

AUTHOR INFORMATION

Corresponding Authors
*(M.B.J.R.) maarten.roeffaers@biw.kuleuven.be
*(B.M.W.) b.m.weckhuysen@uu.nl

Present Addresses
$^\perp$(J.P.H.) Inorganic Materials Chemistry, Eindhoven University of Technology, P.O. Box 513, 5600 MB Eindhoven, The Netherlands.
#(G.D.C.) DSM Ahead BV, Urmonderbaan 22, 6167 RD Geleen, The Netherlands.

Notes
The authors declare no competing financial interest.

ACKNOWLEDGMENTS

REFERENCES

(1) Corma, A. Application of zeolites in fluid catalytic cracking and related processes. In *Studies in Surface Science and Catalysis. Zeolites: Facts, Figures, Future*; Jacobs, P. A., van Santen, R. A., Eds.; Elsevier: Amsterdam, 1989; Vol. 49, pp 49−67.

(2) Rigutto, M. Cracking and hydrocracking. In *Zeolites and Catalysis: Synthesis, Reactions and Applications*; Čejka, J., Corma, A., Zones, S., Eds.; Wiley-VCH: Weinheim, Germany, 2010; pp 547−584.

(3) Stöcker, M. Methanol to olefins (MTO) and methanol to gasoline (MTG). In *Zeolites and Catalysis: Synthesis, Reactions and Applications*; Čejka, J., Corma, A., Zones, S., Eds.; Wiley-VCH: Weinheim, Germany, 2010; pp 687−711.

(4) Lee, C. S.; Park, T. J.; Lee, W. Y. *Appl. Catal. Gen.* **1993**, *96*, 151.

(5) Kramer, G. J.; Van Santen, R. A. *J. Am. Chem. Soc.* **1993**, *115*, 2887.

(6) Boudart, M. *Chem. Rev.* **1995**, *95*, 661.

(7) van den Bergh, J.; Gascon, J.; Kapteijn, F. Diffusion in zeolites—impact on catalysis. In *Zeolites and Catalysis: Synthesis, Reactions and Applications*; Čejka, J., Corma, A., Zones, S., Eds.; Wiley-VCH: Weinheim, Germany, 2010; pp 361−387.

(8) Groen, J. C.; Bach, T.; Ziese, U.; Paulaime-van Donk, A. M.; de Jong, K. P.; Moulijn, J. A.; Pérez-Ramírez, J. *J. Am. Chem. Soc.* **2005**, *127*, 10792.

(9) Michels, N.-L.; Mitchell, S.; Milina, M.; Kunze, K.; Krumeich, F.; Marone, F.; Erdmann, M.; Marti, N.; Pérez-Ramírez, J. *Adv. Funct. Mater.* **2012**, *22*, 2509.

(10) van Donk, S.; Janssen, A. H.; Bitter, J. H.; de Jong, K. P. *Catal. Rev.* **2003**, *45*, 297.

(11) Ong, L. H.; Dömök, M.; Olindo, R.; van Veen, A. C.; Lercher, J. A. *Microporous Mesoporous Mater.* **2012**, *164*, 9.

(12) Zhang, L.; van Laak, A. N. C.; de Jongh, P. E.; de Jong, K. P. Textural characterization of mesoporous zeolites. In *Zeolites and Catalysis: Synthesis, Reactions and Applications*; Čejka, J., Corma, A., Zones, S., Eds.; Wiley-VCH: Weinheim, Germany, 2010; pp 237−282.

(13) Mitchell, S.; Michels, N.-L.; Kunze, K.; Pérez-Ramírez, J. *Nat. Chem.* 2012, 4, 825.

(14) Sklenak, S.; Dĕdeček, J.; Li, C.; Wichterlová, B.; Gábová, V.; Sierka, M.; Sauer, J. *Angew. Chem., Int. Ed.* 2007, 46, 7286.

(15) van Bokhoven, J. A.; van der Eerden, A. M. J.; Koningsberger, D. C. *J. Am. Chem. Soc.* 2003, 125, 7435.

(16) Vjunov, A.; Fulton, J. L.; Huthwelker, T.; Pin, S.; Mei, D.; Schenter, G. K.; Govind, N.; Camaioni, D. M.; Hu, J. Z.; Lercher, J. A. *J. Am. Chem. Soc.* 2014, 136, 8296.

(17) Hall, W. K.; Spiewak, B. E.; Cortright, R. D.; Dumesic, J. A.; Knözinger, H.; Pfeifer, H.; Kazansky, V. B.; Bond, G. C. Characterization of solid catalysts. In *Handbook of Heterogeneous Catalysis*; Ertl, G., Knözinger, H., Weitkamp, J., Eds.; Wiley-VCH: Weinheim, Germany, 1997; pp 689−770.

(18) Aramburo, L. R.; Liu, Y.; Tyliszczak, T.; de Groot, F. M. F.; Andrews, J. C.; Weckhuysen, B. M. *ChemPhysChem* 2013, 14, 496.

(19) van der Bij, H. E.; Cicmil, D.; Wang, J.; Meirer, F.; de Groot, F. M. F.; Weckhuysen, B. M. *J. Am. Chem. Soc.* 2014, 136, 17774.

(20) Mores, D.; Stavitski, E.; Verkleij, S. P.; Lombard, A.; Cabiac, A.; Rouleau, L.; Patarin, J.; Simon-Masseron, A.; Weckhuysen, B. M. *Phys. Chem. Chem. Phys.* 2011, 13, 15985.

(21) Roeffaers, M. B. J.; Ameloot, R.; Baruah, M.; Uji-i, H.; Bulut, M.; De Cremer, G.; Müller, U.; Jacobs, P. A.; Hofkens, J.; Sels, B. F.; De Vos, D. E. *J. Am. Chem. Soc.* 2008, 130, 5763.

(22) Sprung, C.; Weckhuysen, B. M. *J. Am. Chem. Soc.* 2015, 137, 1916.

(23) Stavitski, E.; Weckhuysen, B. M. *Chem. Soc. Rev.* 2010, 39, 4615.

(24) Domke, K. F.; Riemer, T. A.; Rago, G.; Parvulescu, A. N.; Bruijnincx, P. C. A.; Enejder, A.; Weckhuysen, B. M.; Bonn, M. *J. Am. Chem. Soc.* 2012, 134, 1124.

(25) Domke, K. F.; Day, J. P. R.; Rago, G.; Riemer, T. A.; Kox, M. H. F.; Weckhuysen, B. M.; Bonn, M. *Angew. Chem., Int. Ed.* 2012, 51, 1343.

(26) Liu, K.-L.; Kubarev, A. V.; Van Loon, J.; Uji-i, H.; De Vos, D. E.; Hofkens, J.; Roeffaers, M. B. J. *ACS Nano* 2014, 8, 12650.

(27) Weckhuysen, B. M. *Angew. Chem., Int. Ed.* 2009, 48, 4910.

(28) Buurmans, I. L. C.; Weckhuysen, B. M. *Nat. Chem.* 2012, 4, 873.

(29) Zürner, A.; Kirstein, J.; Döblinger, M.; Bräuchle, C.; Bein, T. *Nature* 2007, 450, 705.

(30) Jung, C.; Kirstein, J.; Platschek, B.; Bein, T.; Budde, M.; Frank, I.; Müllen, K.; Michaelis, J.; Bräuchle, C. *J. Am. Chem. Soc.* 2008, 130, 1638.

(31) Roeffaers, M. B. J.; Sels, B. F.; Uji-i, H.; De Schryver, F. C.; Jacobs, P. A.; De Vos, D. E.; Hofkens, J. *Nature* 2006, 439, 572.

(32) Xu, W.; Kong, J. S.; Yeh, Y.-T. E.; Chen, P. *Nat. Mater.* 2008, 7, 992.

(33) Roeffaers, M. B. J.; De Cremer, G.; Libeert, J.; Ameloot, R.; Dedecker, P.; Bons, A.-J.; Bückins, M.; Martens, J. A.; Sels, B. F.; De Vos, D. E.; Hofkens, J. *Angew. Chem., Int. Ed.* 2009, 48, 9285.

(34) Tachikawa, T.; Majima, T. *J. Am. Chem. Soc.* 2009, 131, 8485.

(35) Chen, P.; Zhou, X.; Shen, H.; Andoy, N. M.; Choudhary, E.; Han, K.-S.; Liu, G.; Meng, W. *Chem. Soc. Rev.* 2010, 39, 4560.

(36) De Cremer, G.; Roeffaers, M. B. J.; Bartholomeeusen, E.; Lin, K.; Dedecker, P.; Pescarmona, P. P.; Jacobs, P. A.; De Vos, D. E.; Hofkens, J.; Sels, B. F. *Angew. Chem., Int. Ed.* 2010, 49, 908.

(37) Tachikawa, T.; Majima, T. *Chem. Soc. Rev.* 2010, 39, 4802.

(38) Andoy, N. M.; Zhou, X.; Choudhary, E.; Shen, H.; Liu, G.; Chen, P. *J. Am. Chem. Soc.* 2013, 135, 1845.

(39) Ristanović, Z.; Kerssens, M. M.; Kubarev, A. V.; Hendriks, F. C.; Dedecker, P.; Hofkens, J.; Roeffaers, M. B. J.; Weckhuysen, B. M. *Angew. Chem., Int. Ed.* 2015, 54, 1836.

(40) Roeffaers, M. B. J.; De Cremer, G.; Uji-i, H.; Muls, B.; Sels, B. F.; Jacobs, P. A.; Schryver, F. C. D.; De Vos, D. E.; Hofkens, J. *Proc. Natl. Acad. Sci. U.S.A.* 2007, 104, 12603.

(41) Cordes, T.; Blum, S. A. *Nat. Chem.* 2013, 5, 993.

(42) Janssen, K. P. F.; De Cremer, G.; Neely, R. K.; Kubarev, A. V.; Loon, J. V.; Martens, J. A.; De Vos, D. E.; Roeffaers, M. B. J.; Hofkens, J. *Chem. Soc. Rev.* 2014, 43, 990.

(43) Karwacki, L.; Kox, M. H. F.; de Winter, D. A. M.; Drury, M. R.; Meeldijk, J. D.; Stavitski, E.; Schmidt, W.; Mertens, M.; Cubillas, P.; John, N.; Chan, A.; Kahn, N.; Bare, S. R.; Anderson, M.; Kornatowski, J.; Weckhuysen, B. M. *Nat. Mater.* 2009, 8, 959.

(44) Ristanović, Z.; Hofmann, J. P.; Deka, U.; Schülli, T. U.; Rohnke, M.; Beale, A. M.; Weckhuysen, B. M. *Angew. Chem., Int. Ed.* 2013, 52, 13382.

(45) Aramburo, L. R.; Karwacki, L.; Cubillas, P.; Asahina, S.; de Winter, D. A. M.; Drury, M. R.; Buurmans, I. L. C.; Stavitski, E.; Mores, D.; Daturi, M.; Bazin, P.; Dumas, P.; Thibault-Starzyk, F.; Post, J. A.; Anderson, M. W.; Terasaki, O.; Weckhuysen, B. M. *Chem.—Eur. J.* 2011, 17, 13773.

(46) Dedecker, P.; Duwé, S.; Neely, R. K.; Zhang, J. *J. Biomed. Opt.* 2012, 17, 126008.

(47) Sergé, A.; Bertaux, N.; Rigneault, H.; Marguet, D. *Nat. Methods* 2008, 5, 687.

(48) Niemantsverdriet, J. W. The ion spectroscopies. *Spectroscopy in Catalysis*; Wiley-VCH: Weinheim, Germany, 2007; pp 85−119.

(49) Roeffaers, M. B. J.; Sels, B. F.; Uji-i, H.; Blanpain, B.; L'hoëst, P.; Jacobs, P. A.; De Schryver, F. C.; Hofkens, J.; De Vos, D. E. *Angew. Chem., Int. Ed.* 2007, 46, 1706.

(50) Campbell, S. M.; Bibby, D. M.; Coddington, J. M.; Howe, R. F.; Meinhold, R. H. *J. Catal.* 1996, 161, 338.

(51) Hibbe, F.; Chmelik, C.; Heinke, L.; Pramanik, S.; Li, J.; Ruthven, D. M.; Tzoulaki, D.; Kärger, J. *J. Am. Chem. Soc.* 2011, 133, 2804.

(52) Hibbe, F.; Caro, J.; Chmelik, C.; Huang, A.; Kirchner, T.; Ruthven, D.; Valiullin, R.; Kärger, J. *J. Am. Chem. Soc.* 2012, 134, 7725.

(53) Lu, H. P.; Xun, L.; Xie, X. S. *Science* 1998, 282, 1877.

(54) English, B. P.; Min, W.; van Oijen, A. M.; Lee, K. T.; Luo, G.; Sun, H.; Cherayil, B. J.; Kou, S. C.; Xie, X. S. *Nat. Chem. Biol.* 2006, 2, 87.

(55) Xie, X. S.; Lu, H. P. *J. Biol. Chem.* 1999, 274, 15967.

(56) De Cremer, G.; Roeffaers, M. B. J.; Baruah, M.; Sliwa, M.; Sels, B. F.; Hofkens, J.; De Vos, D. E. *J. Am. Chem. Soc.* 2007, 129, 15458.

(57) Imbihl, R.; Ertl, G. *Chem. Rev.* 1995, 95, 697.

(58) Jensen, K. F.; Ray, W. H. *Chem. Eng. Sci.* 1980, 35, 241.

(59) De Levie, R. *J. Chem. Educ.* 2000, 77, 771.